Chapter 5
Rare Earth Ion Based Luminescence Thermometry

Ilya Kolesnikov and Alina Manshina

Abstract In this chapter, the contactless thermal sensors based on luminescence properties of rare earth-doped nanocrystalline phosphors are discussed. The luminescence thermometry is considered nowadays as a remote and noninvasive approach providing excellent functional parameters—high thermal sensitivity and spatial resolution, wide working temperature range and short response times. The competitive advantage of the luminescence thermometry is its applicability in specific environmental conditions like external electromagnetic field, fast-moving objects, flows and fluids of different nature. The key functional characteristics of temperature sensors are described in the chapter together with different strategies of temperature readout including variants of ratiometric approach via thermally coupled levels, Stark sublevels, spectral line position, and bandwidth and lifetime thermometry. Further progress in this direction includes stimulated market demands and industrial development of micro- and nanoelectronics, photonics, nanomedicine, micro- and nanofluidics, as well as academic interest and scientific challenge in the improvement of current intrinsic limitations. The presented analysis of emerging new directions in the field of luminescence thermometry testifies an interest in widening the working spectral range, development of multi-sensing devices based on multiple emission centers, etc. All these open fascinating prospects of luminescence thermometry in the future and development of even newer fields such as multimodal imaging with temperature monitoring, 3D temperature mapping, and temperature-supervised processes.

I. Kolesnikov (✉) · A. Manshina
Saint Petersburg State University, Saint Petersburg, Russia
e-mail: ilya.kolesnikov@spbu.ru

A. Manshina
e-mail: a.manshina@spbu.ru

K. Yamanouchi et al. (eds.), *Progress in Photon Science*, Springer Series in Chemical Physics 125, https://doi.org/10.1007/978-3-030-77646-6_5

5.1 Introduction

Temperature is one of the fundamental parameters characterizing systems, processes, and phenomena. The notion of temperature is well established from the viewpoint of thermodynamics and used for characterization of various systems (gas, liquid, solid phases, micro and macro objects) in thermodynamic equilibrium. The accurate temperature measurement is necessary for the reliable characterization and control of processes in various fields from biology and medicine to industrial production.

Direct determination of temperature is impossible, but it can be measured via control of various characteristics of bodies such as volume, pressure, conductivity, etc. that are monotonically correlated with temperature change. For convenience, the measurement methods can be classified into three categories, depending on the nature of contact which exists between the sensor and the object of analysis [1]:

- Invasive. The monitoring device is in direct contact with the medium of interest (thermistor- or thermocouple-based technologies).
- Semiinvasive. The medium of interest is treated in some manner to enable remote observation (imaging of thermally sensitive paints).
- Noninvasive. The medium of interest is observed remotely (infrared and luminescence thermography).

Traditional contact thermometers, such as liquid-filled and bimetallic thermometers, thermocouples, pyrometers, and thermistors, are generally not suitable for temperature measurements at scales below 10 μm [2–6]. Moreover, contact measurements require, in general, conductive heat transfer and thus need to reach equilibrium between the sensor and the object. This thermal connection disturbs the temperature of the sample during the measurement, especially for small systems (in which the size is small compared to that of the sensor head) [5].

The rapid technological progress and limitations of contact thermometers for small systems where the spatial resolution decreases to the submicron scale have required the development of new noncontact (semi-invasive and noninvasive) accurate thermometers with micrometric and nanometric spatial resolution [3–5, 7].

Among noninvasive spectroscopic methods for determining temperature, the luminescence thermometry is one of the most promising and accurate techniques. This method provides temperature measurements based on the monitoring of phosphor emission temperature dependence, for example, luminescence intensity (or luminescence intensity ratio, LIR, spectral line position, bandwidth, and excited state lifetime). Luminescence thermometry combines high relative thermal sensitivity ($> 1\%\ K^{-1}$) and spatial resolution (< 10 μm) in short acquisition times (<1 ms), and, as it operates remotely, works even in biological fluids, fast-moving objects, and strong electromagnetic fields [3–5]. Phosphors of different nature have been utilized as contactless thermal sensors through their light emission properties, e.g., polymers [8, 9], DNA or protein conjugated systems [10], organic dyes [11, 12], quantum dots (QDs) [13, 14] transition metals-based materials [15, 16] and rare earth-doped phosphors [17–20].

Rare earth-doped materials are stable and narrow band emitters covering the entire electromagnetic spectrum with, in general, high emission quantum yields (> 50% in the visible range) [21–23]. In the last decade, many of these thermometers have been reported covering a wide temperature range, from cryogenic (T < 100 K) to technological (up to 1200 K) values, and including chelate complexes [24], metal organic frameworks [25, 26], polymers [27], organic–inorganic hybrids [28], and inorganic nanoparticles (NPs) [29–31].

This review focuses primarily on examples of recent successful applications of different temperature dependent luminescence parameters for rare earth-doped inorganic micro and nanoparticles and analysis of future trends in the field of luminescence thermometry.

5.2 Temperature Sensor Performance and Characteristics

For reliable and reproducible temperature monitoring, temperature sensors should be chemically and thermally stable. This is a general requirement to a sensor as a device. As for the estimation of the temperature sensor performance and the comparison of different luminescence thermometers, the following parameters are used:

- thermal sensitivity;
- temperature resolution;
- repeatability and reproducibility.

Absolute (S_a) and relative (S_r) thermal sensitivities are the most common characteristics. The absolute thermal sensitivity shows the absolute change of chosen thermometric parameter with temperature variation and is defined as follows:

$$S_a = \frac{d\Lambda}{dT} \tag{5.1}$$

It is obvious from (5.1) that S_a depends on the absolute Λ value, which can be significantly changed by manipulating the calculation procedure. Therefore, absolute thermal sensitivity cannot be used for fair comparison among different thermometry systems (e.g. mechanical or electrical thermometers) [3]. To compare thermometers irrespective to their nature and sensing parameter, the relative thermal sensitivity is introduced. S_r shows normalized change of chosen thermometric parameter with temperature variation and is defined as follows:

$$S_r = \frac{1}{\Lambda}\frac{d\Lambda}{dT} \tag{5.2}$$

Another important thermometric parameter is the temperature resolution, which provides information about accuracy of thermal sensing that can be derived using this

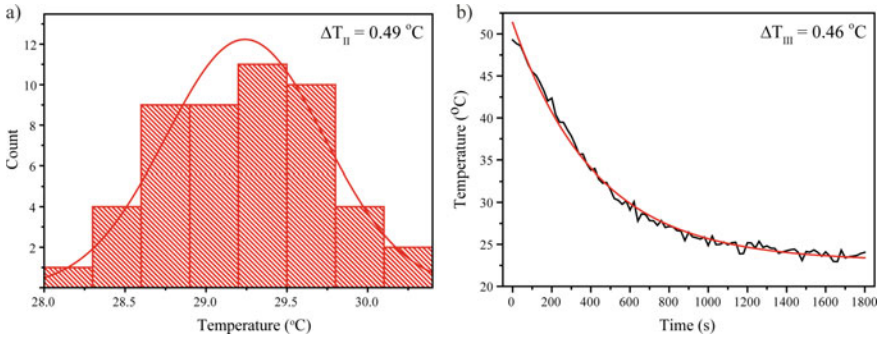

Fig. 5.1 Temperature resolution of YVO_4:Nd^{3+} 3 at.% obtained from **a** acquisition of several consecutive emission spectra at a fixed temperature (ΔT_{II}) and **b** analysis of the thermal relaxation process (ΔT_{III}) [32]

material. There are several experimental techniques to obtain the temperature resolution, which were discussed and compared in our previous work [32]. The temperature resolution can be calculated from calibration curve ($\Delta T_I = \frac{1}{S_r}\frac{\delta\Lambda}{\Lambda}$), from acquisition of several consecutive emission spectra at a fixed temperature (ΔT_{II}), and from the analysis of the thermal relaxation process (ΔT_{III}). It was found that the temperature resolution obtained from abovementioned independent methods gives similar values. For example, temperature resolutions of YVO_4:Nd^{3+} 3 at.% thermometer were determined as follows: $\Delta T_I = 0.72$ °C, $\Delta T_{II} = 0.49$ °C, $\Delta T_{III} = 0.46$ °C (Fig. 5.1) [32].

One interesting strategy to quantify the minimum temperature uncertainty of the thermometer was reported by Alicki and Leitner, in which the spin-boson model was applied and size and system dependent properties were used [33]. For solid-state nanothermometers, the relative fluctuation in temperature is linked to the number of atoms in the sample (N) and its Debye temperature (T_D):

$$\Delta T = \left(\frac{4T}{3\sqrt{3}T_D} e^{\frac{3T_D}{8T}}\right)\frac{1}{\sqrt{N}}T \tag{5.3}$$

For T_D in the range 100–2000 K, the term in parenthesis changes between 0.9 and 1.3, meaning that the order of magnitude of the temperature resolution is determined by $\Delta T = \frac{T}{\sqrt{N}}$ [33], which means that the minimum achievable ΔT is fundamentally controlled by the size of the thermal sensor. In quantum metrology, it is known that for nonentangled particles, the precision $\delta\theta$ of a general quantity θ scales with the inverse of the number of particles (N_P) $\delta\theta = \frac{1}{\sqrt{N_P}}$ [34], a relation called shot-noise scaling (for entangled states, however, Heisenberg-scaling applies and $\delta\theta$ is inversely proportional to N_P). As N_P is proportional to N, the last formula supports the result of the model derived by Alicki and Leitner [33]. There are very few examples reporting the thermal resolution of luminescent thermometers as a function of its size. One case is Alaulamie's work [35] that examined experimentally the correlation between

particle size and the temperature resolution based on the temperature readouts of Er^{3+}-doped up-conversion nanoparticle clusters of different sizes (ranging from 1 to 9 μm). Briefly, the larger the cluster size the higher the signal-to-noise ratio, leading to better temperature resolution (low standard deviation value). The experimental data present an unequivocal increase of the temperature uncertainty as the cluster size decreases according to presented equations.

Thermal sensitivity and *temperature resolution* are important parameters, which take into account both the potential of the temperature probes and the limitation of the experimental setup; it is still possible that other factors contribute to a lower temperature accuracy, such as systematic errors. Repeatability and reproducibility are the two components of precision in a measurement system, and are the major concerns in sensor engineering. Since the great majority of industrial and scientific applications require continuous monitoring, it is critical to achieve the same response under the same external stimulus.

Repeatability refers to the variation in repeat measurements made under identical conditions. A given quantity is considered repeatable if different measurements made using the same instrument or method, over a certain period, give the same results. Variability in measurements made on the same subject in a repeatability study can then be ascribed only to errors due to the measurement process itself [36].

Reproducibility, on the other hand, refers to the variation in measurements of the same measurand carried out under modified conditions [37]. The changing conditions may be due to different measurement methods or instruments being used, measurements being made by different observers, or measurements being made over a period of time within which the "error-free" level of the measurand could undergo nonnegligible change [36].

The repeatability of a thermometric probe indicates the accord between its ability to evaluate the temperature in comparison with a reference temperature probe (a thermocouple, for instance). An acceptable repeatability coefficient can be obtained when the deviation relative to the average measured temperature is lower than double standard deviation of the data. This criterion ensures that, for stochastic processes, 95% of the measurements are less than two standard deviations away from the mean value of temperature.

In a typical procedure, the repeatability of a thermal probe is estimated by cycling the temperature in a given interval, ensuring that each measurement is performed with the probe in thermal equilibrium with the temperature controller. The repeatability of a thermometer's readout upon temperature cycling can be quantified using the expression:

$$R = 1 - \frac{\max(\Delta_c - \Delta_i)}{\Delta_c} \tag{5.4}$$

where Δ_c and Δ_i represent, respectively, the thermometric parameter's mean value and the thermometric parameter measured at each temperature.

Another key feature of the thermometer readout is the ability to reproduce the same results, even when different detectors are employed or the measurements are made in

different ways. Although the reproducibility of a thermometer cannot be numerically quantified, statistical analysis may be used if distinct calibration procedures are significantly different. If the same calibration curve can be obtained in different measurements within the experimental uncertainties of the fitting parameters, it can be concluded than the thermometer produces reproducible readouts under the tested conditions.

5.3 Luminescence Intensity Ratio

Generally, the emission intensity of a given transition is sensitive to temperature changes due to the following mechanisms:

- Population redistribution over electronic levels according to the Boltzmann statistics;
- Temperature-activated quenching mechanisms (e.g., cross-relaxation between electronic levels);
- Nonradiative deactivations (the electrons relax from excited states to the ground state generating heat, instead of light);
- Phonon-assisted Auger conversion processes.

Luminescence thermometers based on the intensity of a single transition are highly dependent of eventual illumination oscillations, signal-to-noise detection, absorption and scatter cross-sections, and local fluctuations on the phosphor concentration. As recursive calibration procedures are not compatible with end-user applications, a ratio of intensities must be employed [2, 5].

The ratiometric thermometry exploits the relative change in the intensity ratio of two independent energy-close transitions. Both emission lines can be generated from a single luminescent center (single-center thermometers), or they can result from two distinct emitting centers (dual-center thermometers) [3, 4]. To date, majority of the reported ratiometric luminescence thermometers are single-center thermometers.

In single-center ratiometric thermometers, Δ (or LIR) is defined using the emission intensities of the $|2\rangle \rightarrow |0\rangle$ (I_2) and $|1\rangle \rightarrow |0\rangle$ (I_1) transitions, where $|0\rangle$ denotes the ground level and $|1\rangle$ and $|2\rangle$ the two thermally coupled excited levels (level $|2\rangle$ is more energetic than level $|1\rangle$) [38–40],

$$\Delta = \frac{I_2}{I_1} = \frac{A_{02} h \nu_{02} N_2}{A_{01} h \nu_{01} N_1} \tag{5.5}$$

where N_1 and N_2 are the populations of the $|1\rangle$ and $|2\rangle$ levels, ν_{01} and ν_{02} are the frequencies of the $|1\rangle \rightarrow |0\rangle$ and $|2\rangle \rightarrow |0\rangle$ transitions, and A_{01} and A_{02} are the total spontaneous emission rates from levels $|1\rangle$ and $|2\rangle$ to level $|0\rangle$. If the depopulation of the $|1\rangle$ and $|2\rangle$ energy levels involves other energy levels beyond $|0\rangle$, (5.5) must be corrected by the β_2/β_1 ratio, where β_i ($i = 1, 2$) are the branching ratios of the $|i\rangle$ level, i.e., the percentage of the total emission from the thermalized level ($|1\rangle$ or

$|2\rangle$) to the final $|0\rangle$ state. If the two high-energy levels are in thermal equilibrium (they are called "thermally coupled levels," with energy separations of the order of the thermal energy kT), N_1 and N_2 are related by

$$N_2 = \frac{g_2}{g_1} N_1 \exp\left(-\frac{\Delta E}{kT}\right) \tag{5.6}$$

where g_1 and g_2 are the degeneracies of the two levels and ΔE is the energy gap between the barycenters of the $|1\rangle \rightarrow |0\rangle$ and $|2\rangle \rightarrow |0\rangle$ emission bands. Equation (5.5) is, thus, written as

$$\Delta = \frac{g_2 A_{02} h\nu_{02}}{g_1 A_{01} h\nu_{01}} \exp\left(-\frac{\Delta E}{kT}\right) = B \exp\left(-\frac{\Delta E}{kT}\right) \tag{5.7}$$

with $B = \frac{g_2 A_{02} h\nu_{02}}{g_1 A_{01} h\nu_{01}}$. The two light-emitting levels cannot be too separated in energy, otherwise its thermalization is not detected. Typically, they are considered "thermally coupled" (e.g., in a thermodynamically quasi equilibrium state) for ΔE ranging from 200 to 2000 cm^{-1} [41]. As thermally coupled levels could be two excited electron energy levels or ground electronic energy levels, or two Stark sublevels.

Technically, LIR is calculated as the ratio between integral intensities of two emission transitions. This standard calculation technique can be named peak-to-peak ratio. It was found that temperature change sometimes affects the valley between emission bands more significantly than the bands themselves. Thus, monitoring peak-to-valley ratio could result in more sensitive thermal sensing in such a case. Comparison of peak-to-peak and peak-to-valley ratios would be conducted in terms of thermometric performances.

5.3.1 Excited Thermally Coupled Levels

An example of using excited thermally coupled levels for ratiometric thermometry in wide temperature range of 123–873 K is descried below, in which thermal sensing was performed with YVO_4:Nd^{3+} 2.4 at.% NPs [42]. Room temperature excitation and emission spectra of YVO_4:Nd^{3+} 2.4 at.% NPs are presented in Fig. 5.2a. As can be seen, excitation spectrum consists of bands situated at 420–442, 455–490, 500–550, 550–640, and 670–700 nm, which are ascribed to the transitions from ground state $^4I_{9/2}$ to higher levels $^2D_{5/2}$, $^4G_{9/2} + {}^4G_{11/2} + {}^2K_{15/2}$, $^4G_{7/2} + {}^4G_{9/2} + {}^2K_{13/2}$, $^4G_{5/2} + {}^4G_{7/2} + {}^2H_{11/2}$, $^4F_{9/2}$, respectively [43, 44]. Emission spectrum consists of narrow lines attributed to the $^4F_{3/2} - {}^4I_{9/2}$ (870–925 nm) and $^4F_{5/2} + {}^2H_{9/2} - {}^4I_{9/2}$ (790–850 nm) transitions. The energy levels scheme of Nd^{3+} ion in YVO_4 host displaying thermally coupled $^4F_{3/2}$ and $^4F_{5/2} + {}^2H_{9/2}$ levels is presented in Fig. 5.2b.

The temperature dependence of emission spectrum of YVO_4:Nd^{3+} 2.4 at.% NPs is shown in Fig. 5.3a. One can see that intensity ratio between $^4F_{5/2} - {}^4I_{9/2}$ (808 nm)

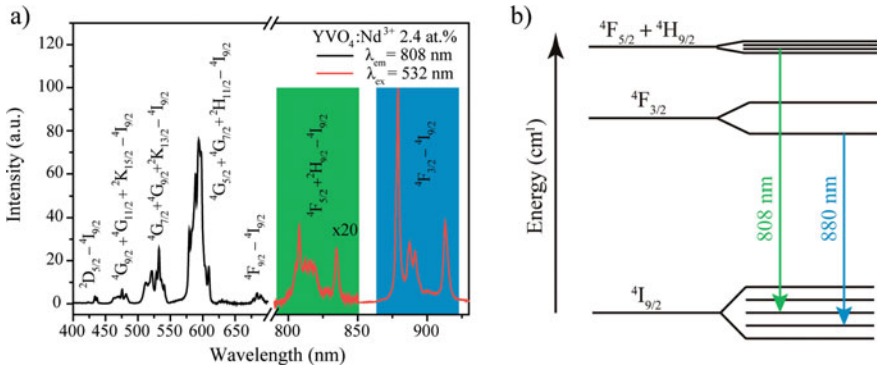

Fig. 5.2 **a** Excitation (black) and emission (red) spectra of YVO_4:Nd^{3+} 2.4 at.% NPs (λ_{em} = 880 nm, λ_{ex} = 532 nm) at room temperature; **b** energy levels scheme of Nd^{3+} ion in YVO_4 host [42]

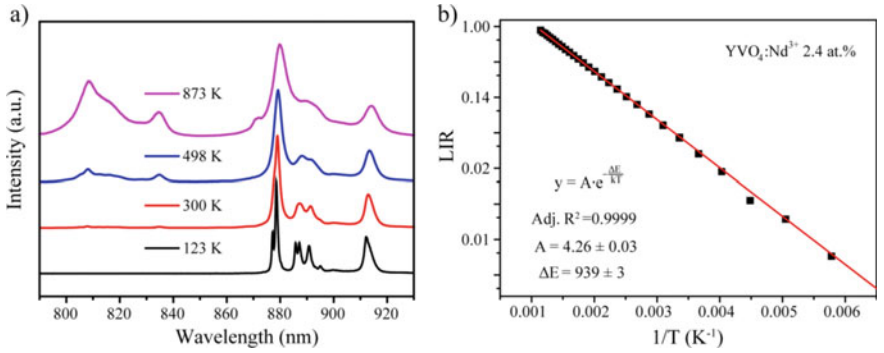

Fig. 5.3 **a** Emission spectra of YVO_4:Nd^{3+} 2.4 at.% at different temperatures (T = 123 K; 300 K; 498 K; 873 K); **b** temperature dependence of LIR between the emission peaks at 808 nm ($^4F_{5/2} - {}^4I_{9/2}$) and 880 nm ($^4F_{3/2} - {}^4I_{9/2}$) for YVO_4:Nd^{3+} 2.4 at. % NPs [42]

and $^4F_{3/2} - {}^4I_{9/2}$ (880 nm) transitions is significantly changed and can be used as thermometric parameter. Taking into account the energy gap between the excited levels and (5.7), we can write $\Delta = \frac{I_{808}}{I_{880}} = A \cdot \exp\left(-\frac{\Delta E}{kT}\right)$. Figure 5.3b shows evolution of LIR as a function of temperature on semi-logarithmic scale. The observed experimental data is accurately fitted by the exponential Boltzmann formula with Adj. R^2 = 0.99. Therefore, monitoring this spectral ratio could provide information about temperature around YVO_4:Nd^{3+} NPs and could be used for different applications.

Relative thermal sensitivity of YVO_4:Nd^{3+} 2.4 at.% NPs obtained according to (5.2) was found to be 1.5% K^{-1}. This value is comparable with other Nd^{3+} based thermometers. For example, sensitivity of Gd_2O_3:Nd^{3+} NPs based on LIR between $^4F_{5/2} - {}^4I_{9/2}$ and $^4F_{3/2} - {}^4I_{9/2}$ transitions was determined to be 1.75% K^{-1} at 288 K [45]. Nd^{3+}-doped $NaYF_4$ microcrystals showed maximum sensitivity of 1.12% K^{-1} at the temperature 500 K [46]. In works [47] and [48], the authors presented $CaWO_4$ and

La_2O_2S bulk powders doped with Nd^{3+} ions, and the maximum of S_r was about 0.3% K^{-1} at the temperature 668 K and 1.1% K^{-1} at the temperature 358 K, respectively.

As YVO_4:Nd^{3+} 2.4 at.% NPs can be used for thermal sensing in a wide temperature range, temperature resolution was obtained at significantly different temperatures (313 and 673 K) suitable for biological and technical applications. Temperature resolutions calculated from calibration curves were determined to be 0.5 K and 1.2 K for 313 K and 673 K temperatures, respectively. The temperature resolution of other Nd^{3+} based thermometers were reported as follows: 0.14 K at 288 K (Gd_2O_3:Nd^{3+}) [45], 2 K at 298 K (LaF_3:Nd^{3+}), [49] 1.13 K at 313 K ($LiNdP_4O_{12}$) [50]. So, we can draw a conclusion that the thermometric performances of YVO_4:Nd^{3+} 2.4 at.% NPs is comparable with other Nd^{3+}-doped thermal sensors.

Another example of contactless ratiometric sensing based on the LIR between transitions originated from two thermally-coupled excited electron levels is shown by Dy^{3+}-doped YVO_4 nanophosphors [51]. Normalized emission spectra of YVO_4:Dy^{3+} 1 at.% nanopowders measured at different temperatures (298, 423 and 673 K) are presented in Fig. 5.4a. The observed emission lines are originated from electron transitions from $^4I_{15/2}$ and $^4F_{9/2}$ excited states with energy separation of about 1000 cm^{-1} (Fig. 5.4b). According to definition, $^4I_{15/2}$ and $^4F_{9/2}$ are thermally coupled levels, and therefore, a ratiometric approach for transitions from these excited states can be utilized to determine the local temperature. The LIR between $^4I_{15/2} - {}^6H_{15/2}$ and $^4F_{9/2} - {}^6H_{15/2}$ transitions ($LIR_{455/480}$), as well as the ratio between $^4I_{15/2} - {}^6H_{15/2}$ and $^4F_{9/2} - {}^6H_{13/2}$ transitions ($LIR_{455/575}$) were used for thermal sensing.

The variations of the LIR values of YVO_4:Dy^{3+} 1 at.% nanocrystalline powders as a function of the temperature are presented in Fig. 5.5a, b. Temperature induced

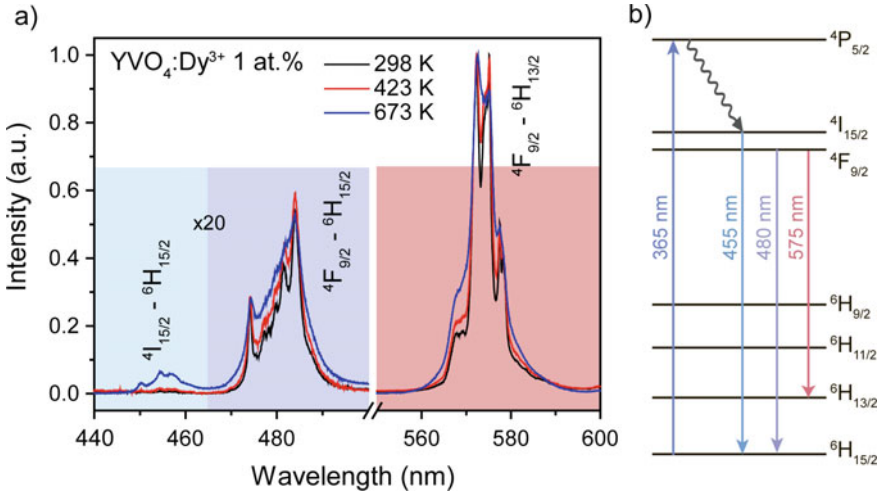

Fig. 5.4 Normalized emission spectra of **a** YVO_4:Dy^{3+} 1 at.% and **b** YVO_4:Dy^{3+} 2 at.% nanopowders at different temperatures. The colored areas are used for the integral intensity ratio calculations. **c** Energy levels scheme of YVO_4:Dy^{3+} nanophosphors [51]

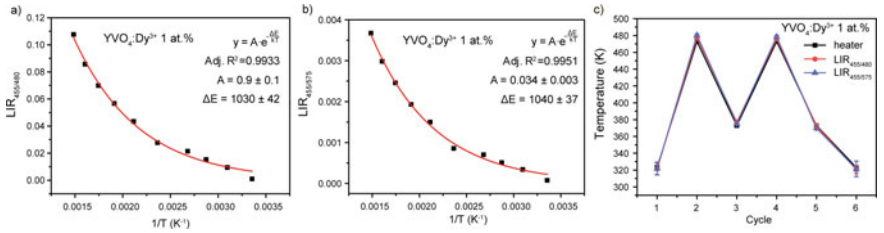

Fig. 5.5 Luminescence intensity ratio **a** $LIR_{455/480}$ and **b** $LIR_{455/575}$ of $YVO_4:Dy^{3+}$ 1 at.% nanopowders as a function of temperature [51]

change of LIR is caused by electron re-distribution at the energy levels according to the Boltzmann formula (5.7).

Performance of $YVO_4:Dy^{3+}$ 1 at.% thermometer is studied in terms of thermal sensitivities, temperature resolution, and repeatability. The observed temperature dependences of S_a and S_r demonstrate opposite behavior: the temperature increase leads to a gradual growth of S_a and a monotonic decline of S_r. As the temperature dependence in both LIRs originate from the same excited levels: $^4I_{15/2}$ and $^4F_{9/2}$, it is not surprising that the maximal relative thermal sensitivity ($T = 298$ K) for $LIR_{455/480}$ and $LIR_{455/575}$ ratios is similar: 1.8% K^{-1} ($YVO_4:Dy^{3+}$ 1 at.%). However, the absolute thermal sensitivities differ significantly: 0.039 K^{-1} at 673 K ($LIR_{455/480}$) and 0.0013 K^{-1} at 673 K ($LIR_{455/575}$). Compared to Er^{3+}, Tm^{3+} or Nd^{3+} ions, the use of dysprosium ions for temperature sensing are relatively rare. Among other Dy^{3+} single doped materials, the obtained S_r values are comparable to the values reported in the literature: 1.7% K^{-1} for $BaYF_5:Dy^{3+}$ NPs [52], 1.6% K^{-1} for $Gd_2Ti_2O_7:Dy^{3+}$ NPs [53], 1.7% K^{-1} for YAG:Dy^{3+} microcrystals [54], 1.7% K^{-1} and 1.3% K^{-1} for Dy:Y$(acac)_3$ and Dy:Y$(acac)_3$(phen) molecular crystals, respectively [55].

Temperature resolution of $YVO_4:Dy^{3+}$ 1 at.% thermometer was estimated from consecutive emission spectra measured at fixed heating stage temperature. Due to the rather wide temperature sensing region, ΔT was obtained for 323 and 473 K. The obtained value lay in the range of 3–7 K depending on the measured temperature and the luminescence intensity ratio used.

Repeatability of $YVO_4:Dy^{3+}$ thermometer was tested over cyclic heating-cooling measurements (Fig. 5.5c). During the experiment, we increased and decreased the temperature within the thermal range of 323–473 K. Black squares indicate the actual temperature of heater, whereas red circles and blue triangles present temperature obtained with $LIR_{455/480}$ and $LIR_{455/575}$ luminescence intensity ratio, respectively. Taking into account temperature uncertainties, we can conclude that the considered $YVO_4:Dy^{3+}$ nanopowder has good repeatability: temperatures obtained using optical thermometry are repeated from cycle to cycle and they are in good agreement with the actual heater temperature.

5.3.2 Ground Thermally Coupled Levels

In addition to excited levels with energy gap not exceeding 2000 cm^{-1}, the thermoequilibrium between the two ground energy levels can be used for ratiometric thermometry. This strategy was successfully demonstrated using $^7F_0$, $^7F_1$, and $^7F_2$ europium ground levels in $YVO_4:Eu^{3+}$ nanophosphors [56]. It was notably the first demonstration of thermal sensing based on excitation spectra of luminescence nanoparticles.

Excitation spectra of $YVO_4:Eu^{3+}$ 16 at.% NPs monitored at forced electric dipole transition $^5D_0$–$^7F_4$ (698 nm) measured at different temperatures are shown in Fig. 5.6a. The studied temperature range was 299–466 K. These spectra consist of many bands, which can be used for thermal sensing based on electron population redistribution of low lying levels. As $^7F_0$, $^7F_1$, and $^7F_2$ levels are situated within 2000 cm^{-1}, the following luminescence lines were utilized to calculate LIR: $^7F_0$–$^5D_1$ (526 nm), $^7F_1$–$^5D_1$ (537 nm), $^7F_2$–$^5D_1$ (555 nm), $^7F_1$–$^5D_0$ (593 nm), and $^7F_2$–$^5D_0$ (613 nm) (Fig. 5.6b). LIRs based on thermal electron population redistribution between $^7F_0$ and $^7F_1$, $^7F_0$ and $^7F_2$, $^7F_1$ and $^7F_2$ levels were compared. Moreover, effect of excited level on LIR sensing properties was also studied. The following

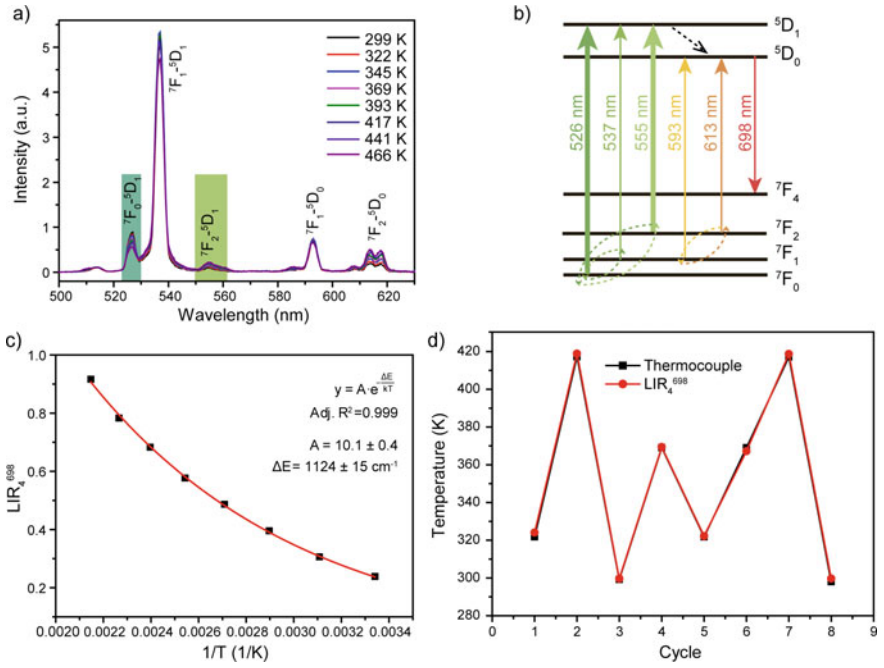

Fig. 5.6 **a** Excitation spectra of $YVO_4:Eu^{3+}$ 16 at.% NPs obtained at different temperatures (λ_{em} = 698 nm); **b** thermal sensing scheme based on excitation spectra of $^5D_0$–$^7F_4$ transition, **c** temperature evolution of luminescence intensity ratio LIR_4^{698}; **d** complex heating-cooling cycles [56]

luminescence intensity ratios were calculated: $^7F_1$–$^5D_1$/$^7F_0$–$^5D_1$ (LIR_1^{698}), $^7F_1$–$^5D_0$/$^7F_0$–$^5D_1$ (LIR_2^{698}), $^7F_2$–$^5D_1$/$^7F_0$–$^5D_1$ (LIR_3^{698}), $^7F_2$–$^5D_0$/$^7F_0$–$^5D_1$ (LIR_4^{698}), $^7F_2$–$^5D_1$/$^7F_1$–$^5D_1$ (LIR_5^{698}), and $^7F_2$–$^5D_0$/$^7F_1$–$^5D_1$ (LIR_6^{698}). Integral intensity of each band was collected within spectral range equal to spectral slit width during measurement (3 nm). In all cases experimental data were fitted by the exponential function (5.7), which confirmed that LIR thermal dependence is governed by a Boltzmann process. All suggested LIRs are suitable to provide thermal sensing. A comparison of the effective gap ΔE_{eff} obtained from the fitting procedure led to a conclusion that LIR_4^{698} has the best thermometric performances among all calculated $LIRs_4^{698}$. A calibration curve of the most promising R_4^{698} for YVO_4:Eu^{3+} 16 at.% nanophosphor is shown in Fig. 5.6c. The highest S_r value of YVO_4:Eu^{3+} 16 at.% NPs was 1.25% K^{-1} at 298 K, while S_a achieved 0.00475 K^{-1} at 466 K. Temperature resolution was found to be 1 K at 323 K, which was obtained from the calibration curve. To monitor the repeatability, a thermal cycling experiment with YVO_4:Eu^{3+} 16 at.% nanophosphor, where the temperature was determined in consecutive complex heating-cooling cycles, was carried out. The temperature was defined by two independent methods: luminescence nanothermometry (LIR_4^{698}) and thermocouple measurements. As can be seen from Fig. 5.6d, measured and calculated temperatures are in good agreement taking into account thermal uncertainties.

5.3.3 Stark Sublevels

LIR can be calculated not only by using different excited or ground electronic levels, but also by utilizing different Stark sublevels. As the energy gap between Stark sublevels is less than that between the electronic levels, relative sensitivity of thermometers based on this approach is lower. However, some thermometry applications require two emission bands used for LIR calculation within a certain spectral region, for example, biological optical transparency windows, which is of crucial importance for medicine and biology. This requirement can be fulfilled by Nd^{3+}-doped Y_2O_3 NPs possessing emission peaks originated from different Stark sublevels and situated in both first (650–950 nm) and second (1000–1350 nm) biological windows (BW) [57]. Detailed emission spectra of Y_2O_3:Nd^{3+} 1 at.% NPs at different temperatures (26.5 and 58.5 °C) measured in the spectral range of 870–922 nm (I-BW) are presented in Fig. 5.7a. The luminescence intensity ratio between $^4F_{3/2}(2) - {}^4I_{9/2}(3)$ and $^4F_{3/2}(1) - {}^4I_{9/2}(3)$ (hereafter denoted as LIR_1^I) was chosen for nanothermometry (Fig. 5.7b), because it should have a temperature dependence in biological range due to the value of the energy gap between the Stark sublevels. As can be seen, the emission lines used for thermal sensing are well resolved, thus, a deconvolution analysis is not required. Temperature evolution of LIR_1^I demonstrated a monotonous pseudo-linear trend within the studied temperature range (Fig. 5.7c). The observed pseudo-linear trend appeared from usual Boltzmann function with small energy gap in the narrow temperature range.

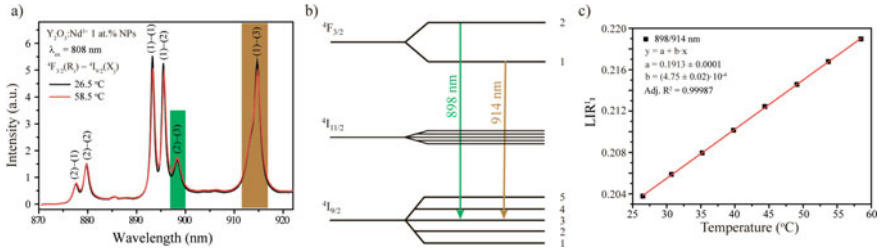

Fig. 5.7 **a** Emission spectra of Y_2O_3:Nd^{3+} 1 at.% nanoparticles obtained at two different temperatures ($\lambda_{ex} = 808$ nm); **b** energy levels scheme of transition $^4F_{3/2}(R_i) - {}^4I_{9/2}(X_j)$ for Nd^{3+} ion in the Y_2O_3 host; **c** luminescence intensity ratios LIR_1^I as a function of temperature [57]

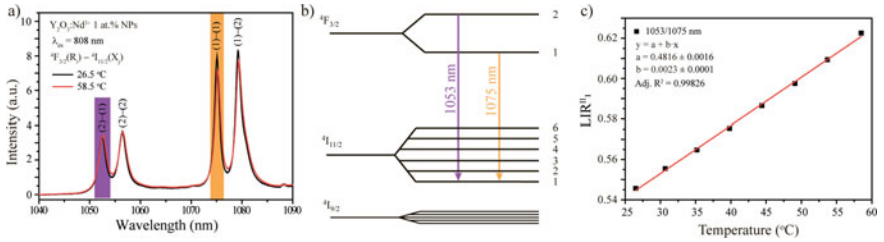

Fig. 5.8 **a** Emission spectra of Y_2O_3:Nd^{3+} 1 at.% nanoparticles obtained at different temperatures ($\lambda_{ex} = 808$ nm); **b** energy levels scheme of transition $^4F_{3/2}(R_i) - {}^4I_{11/2}(Y_k)$ for Nd^{3+} ion in the Y_2O_3 host; **c** luminescence intensity ratios LIR_1^{II} as a function of temperature [57]

Thermal sensing using Y_2O_3:Nd^{3+} 1 at.% NPs was also performed in the II-BW. Detailed emission spectra at different temperatures (26.5 and 58.5 °C) measured in the spectral range of 1040–1090 nm are presented in Fig. 5.8a. Nanothermometry was based on the luminescence intensity ratio between $^4F_{3/2}(2) - {}^4I_{11/2}(1)$ and $^4F_{3/2}(1) - {}^4I_{11/2}(1)$ (hereafter denoted as LIR_1^{II}) (Fig. 5.8b). Figure 5.8c showed LIR_1^{II} as a function of temperature from which a pseudo-linear behavior was observed.

The relative thermal sensitivities of Y_2O_3:Nd^{3+} 1 at.% NPs were found to be 0.23 and 0.43% $°C^{-1}$ for Stark sublevels LIR_1^I and LIR_1^{II}, respectively. Careful examination of earlier reported Stark sublevel-based LIR for other Nd^{3+}-doped thermometers ($NaYF_4$, YAG, $YNbO_4$, LaF_3, YVO_4, $KGd(WO_4)_2$, CaF_2) led to a conclusion that among NIR-to-NIR nanothermometers, Y_2O_3:Nd^{3+} nanophosphor demonstrates the best relative thermal sensitivity. Sub-degree temperature resolution (0.2 and 0.5 °C for LIR_1^I and LIR_1^{II}, respectively) makes Nd^{3+}-doped Y_2O_3 NPs prospective candidates for accurate thermal sensing.

5.3.4 Peak-to-Valley Calculation

As it was demonstrated in the previous paragraphs, ratiometric thermal sensing can be successfully performed using emission transition originated from different Stark sublevels despite the much lower relative thermal sensitivity compared to that of the different electronic levels. To enhance thermal sensitivity, a new strategy based on the monitoring of peak-to-valley ratio was developed [32].

Normalized emission spectra generated upon 808 nm excited YVO_4:Nd^{3+} 3 at.% NPs obtained at 26 and 58 °C are shown in Fig. 5.9a. A temperature increase results in the increase of the relative contribution of the $^4F_{3/2}(2) - {}^4I_{11/2}(3)$ transition due to temperature induced population of $^4F_{3/2}(2)$ Stark sublevel [58]. The intensity ratio of $^4F_{3/2}(1) - {}^4I_{11/2}(1)$ (1064.8 nm) and $^4F_{3/2}(2) - {}^4I_{11/2}(3)$ (1072 nm) transitions (hereafter denoted as LIR_3) has been previously used for nanothermometry [58]. As it can be clearly seen from Fig. 5.9, temperature change also significantly affects relative intensity of "valleys" centered at 1066.3 and 1063.7 nm. Therefore, luminescence intensity ratios between the largest peak at 1064.8 nm and the valley at 1066.3 nm (LIR_1) or the valley at 1063.7 nm (LIR_2) were used for thermal calibration to enhance thermal sensitivity.

The intensity ratio demonstrated a monotonous pseudo-linear trend in the biophysical temperature range (25–60 °C) for all LIRs (Fig. 5.10). Strictly speaking, luminescence intensity ratio should be fitted by the exponential Boltzmann formula, but it was much more convenient to use a linear function to define local temperature from the observed ratio [59–61].

Calculated thermal sensitivities for different LIRs gave the following values: 0.35, 0.32 and 0.20% K^{-1}. A simple analysis showed that the new strategy for LIR calculation (peak-to-valley) results in a remarkable enhancement up to 1.75 of the thermal sensitivity compared to standard approach (peak-to-peak). Moreover, the new strategy also significantly improved another important thermometric

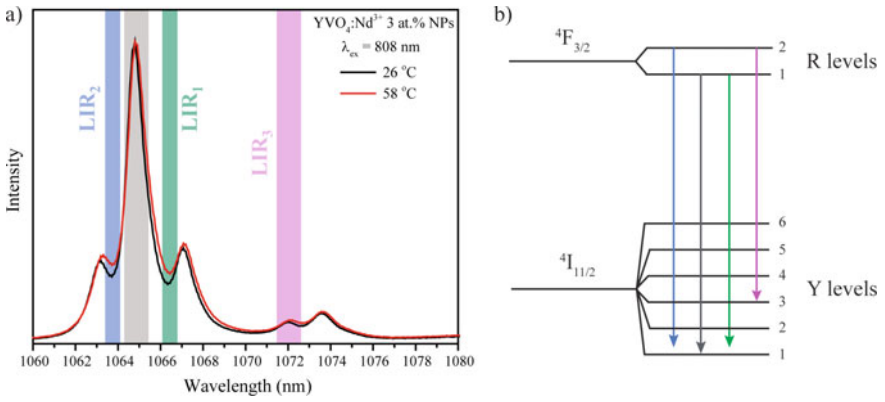

Fig. 5.9 **a** Normalized emission spectra of YVO_4:Nd^{3+} 3 at.% NPs obtained at different temperatures ($\lambda_{ex} = 808$ nm); **b** energy levels scheme of Nd^{3+} ion in the YVO_4 host [32]

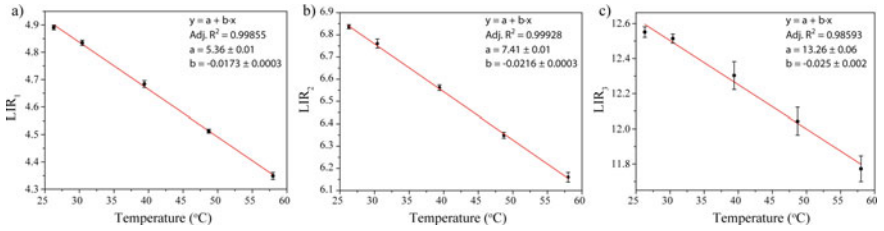

Fig. 5.10 **a** Evolution of the integral intensity ratio between emission peak 1064.8 nm and valley 1066.3 nm; **b** evolution of the integral intensity ratio between emission peak 1064.8 nm and valley 1063.7 nm; **c** evolution of the integral intensity ratio between 1064.8 and 1072 nm emission peaks. Red line corresponds to the best fitting [32]

performance, temperature resolution. ΔT was obtained using all three techniques described above. However, here we provide calibration curve method. It was found that the temperature resolution of YVO_4:Nd^{3+} 3 at.% equals 0.6, 0.7 and 2.3 °C, when monitoring LIR_1, LIR_2 and LIR_3, respectively. We can therefore conclude that the peak-to-valley strategy enhances accuracy of thermal sensing of NIR-to-NIR ratiometric thermometer by 4 times.

5.4 Spectral Line Position Thermometry

This technique is based on the analysis of the spectral positions of the emission lines, which are unequivocally determined by the energy separation between the two electronic levels involved in the emission. Any temperature change leads to modifications in the arrangement of the lattice ions surrounding rare earth ion and, therefore, to a crystal field modification which results in a shift in the emission lines. Temperature reading can be achieved by an accurate spectral analysis of the emission lines. Typically, in the physiological range, these temperature-induced shifts are small but they can be recognized when dealing with rare earth ions characterized by narrow emission lines, such as neodymium [62].

Generally, an increase in temperature leads to the red shift of the emission line positions. When the crystal temperature is increased, the energy levels and, therefore, the spectral lines broaden, invariably as the higher phonon modes are occupied. Since there are many high-lying energy levels which couples, an energy level is normally lowered. Further, it is usually the case that the temperature dependence of higher levels is larger than for lower levels because of smaller energy denominators. As a result, the spectral lines are observed to shift normally to the longer wavelengths when the temperature is increased [63, 64]. Thermal shifts to the blue can be caused by thermal expansion of the crystal lattice due to the changes of crystalline-field strength and impurity-level energies. Such shifts were observed for some transitions of Nd^{3+} in the soft hydrated crystal $Pr(NO_3)_3 \cdot 6H_2O$. However, such thermal expansion is negligible in hard ionic crystals [63, 64].

The shift of the emission line is usually associated with the electron–phonon coupling effect, which results from the fact that at higher temperatures, host vibration modes introduce random perturbation of the ion's local environment [65]. According to the phonon theory [66, 67], the line position is affected by the crystal strain inhomogeneity, direct one-phonon processes, multiphonon processes, and Raman phonon scattering processes. As found in earlier studies [64, 68], thermal shift is mainly governed by electron–host interaction effect associated with Raman scattering, and therefore the simplified theoretical expressions for the line shift can be written in the following form [69]:

$$\upsilon = \upsilon_0 + \alpha\left(\frac{T}{\Theta_D}\right)^4 \int_0^{\Theta_D/T} \frac{x^3}{e^x - 1} dx \tag{5.8}$$

where υ_0, α, Θ_D represent the initial line position (determined at low temperature, in this paper at 123 K), the electron–host coupling parameter, and the effective Debye temperature, respectively.

Spectral line position thermometry was demonstrated by use of YVO_4:Nd^{3+} 2.4 at % NPs possessing narrow emission lines [70]. Normalized emission spectra of this phosphor obtained at different temperatures in a wide range of 123–873 K are shown in Fig. 5.11a. The position of the most intensive emission band, which is attributed to the transition between the Stark levels of the $^4F_{3/2}$ and $^4I_{11/2}$ states was chosen as a temperature dependent parameter. The growth of temperature from 123 to 873 K caused monotonical red shift of the emission line position which can be perfectly fitted by (5.8) (red curve in Fig. 5.11b).

It should be noted that, in spite of its clear physical meaning, the aforementioned function cannot be used for thermal sensing due to its complexity and inability

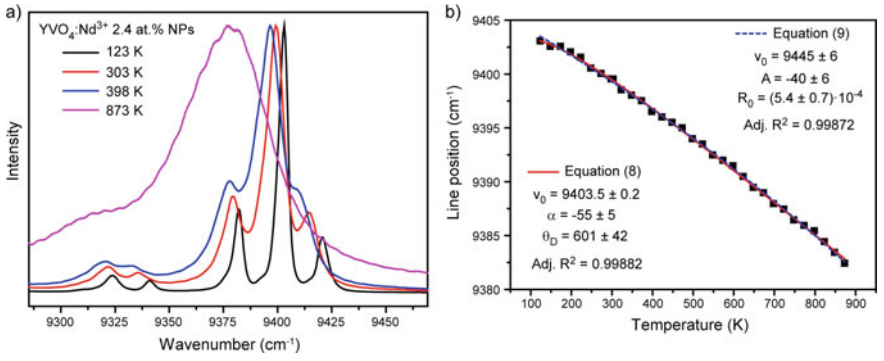

Fig. 5.11 **a** Normalized emission spectra of $^4F_{3/2} - {}^4I_{11/2}$ transition obtained at different temperatures (123–873 K); **b** line position of $^4F_{3/2}$ (R_1) $- {}^4I_{11/2}$ (Y_1) transition as a function of temperature [70]

to derive temperature as a function of spectral shift. Therefore, a simple exponential expression was suggested for fitting the observed line shift as a function of temperature:

$$\upsilon = \upsilon_0 + A \cdot e^{R_o T} \tag{5.9}$$

Both fitting procedures resulted in similar values of adjusted R^2: 0.99882 and 0.99872 for (5.8) and (5.9), respectively. Therefore, the proposed fitting function allows us to use a spectral shift of emission line for thermal sensing.

Relative thermal sensitivity based on line shift of YVO_4:Nd^{3+} 2.4 at % NPs was found to be 0.75% K^{-1} at 303 K, which is much higher than S_r of $LiLaP_4O_{12}$:Nd^{3+} 1% NPs (0.47% K^{-1}) and $LiNdP_4O_{12}$ NPs (0.003% K^{-1}).

5.5 Bandwidth Thermometry

Emission line bandwidth is determined by the properties of the material such as the degree of disorder and temperature. Generally, the emission lines of phosphors broaden as the temperature increases. This is ascribed to the intrinsic vibrations of the lattice exhibiting homogeneous broadening, which depends sensitively on temperature or to the presence of different optical centers and defects exhibiting inhomogeneous broadening, which depends only slightly on temperature. Detailed analysis of thermally-induced broadening in rare earth-doped inorganic NPs as well as temperature sensing based on line bandwidth is demonstrated in [71].

Bandwidth is affected by the same processes which influence line position. According to the phonon theory [66], the width of energy level is given by:

$$\Delta\upsilon = \Delta\upsilon^{strain} + \Delta\upsilon^{D} + \Delta\upsilon^{M} + \Delta\upsilon^{R} \tag{5.10}$$

The first term, $\Delta\upsilon^{strain}$, is the width due to the crystal strains. The second term, $\Delta\upsilon^{D}$, is the width due to direct one-phonon process between the selected energy level and other nearby levels, and consists of a temperature-independent part, which is due to a spontaneous one-phonon emission, and a temperature-dependent part. The third term, $\Delta\upsilon^{M}$, is the contribution to the width from the multiphonon emission processes, which are temperature independent. The last term, $\Delta\upsilon^{R}$ represents the width for the Raman multiphonon process associated with phonon scattering by impurity ions [72]. It should be noted that the first term represents inhomogeneous broadening with a Gaussian line shape due to crystal strains, whereas the other terms give rise to homogeneous broadening with a Lorentzian line shape. Since different line shapes are expected for several broadening mechanisms, simple summation of (5.4) is a rough approximation, and a line shape composed of both homogeneous and inhomogeneous parts can be represented by a Voigt profile [73]. If it is necessary, line width may be resolved into homogeneous and inhomogeneous contributions by using the numerical tables prepared by Posener [74].

It was earlier found that the main contribution to line broadening is Raman scattering process which consists of the absorption of one phonon and the emission of another phonon without changing the electronic state of the ion [64, 72]. In this case, the width of the energy level can be given by following expression:

$$\Delta\upsilon = \Delta\upsilon_0 + \overline{\alpha}\left(\frac{T}{\Theta_D}\right)^7 \int_0^{\Theta_D/T} \frac{x^6 e^x}{(e^x - 1)^2} dx \tag{5.11}$$

where $\Delta\upsilon_0$ is the initial linewidth, $\overline{\alpha}$ is the coupling coefficient for the electron–phonon interaction, and Θ_D is the effective Debye temperature.

Normalized emission spectra of Y_2O_3:Nd^{3+} 1 at.% NPs obtained at different temperatures in a wide range of 123–873 K are presented in Fig. 5.12a. Bandwidth of $^4F_{3/2}(R_1)$–$^4I_{11/2}(Y_1)$ transition was monitored to obtain thermal sensing. Due to the proximity of other emission lines, deconvolution procedure was performed to define the exact bandwidth. An evolution of the full width at half maximum (FWHM) of the emission line as a function of temperature is presented in Fig. 5.12b. Experimental data were approximated with (5.11) with previously defined effective Debye temperature $\Theta_D = 538$ K. Similar to line position sensing, (5.11) was not suitable for the calibration of the luminescence thermometer. Therefore, the experimental data were perfectly fitted with simple exponential expression:

$$\Delta\upsilon = \Delta\upsilon_0 + A \cdot e^{R_o T} \tag{5.12}$$

Bandwidth relative thermal sensitivity of Y_2O_3:Nd^{3+} 1 at % NPs was 0.36% K^{-1} at 298 K, which is comparable with S_r of other Nd^{3+}-doped nanothermometers: $LiLaP_4O_{12}$:Nd^{3+} 1% (0.32% K^{-1}), $LiNdP_4O_{12}$ (0.46% K^{-1}) and YVO_4:Nd^{3+} 2.4 at.% (0.14% K^{-1}). Temperature sensing based on bandwidth demonstrated superior accuracy in a wide temperature range: 0.2 K at 323 K and 0.5 K at 498 K. It is

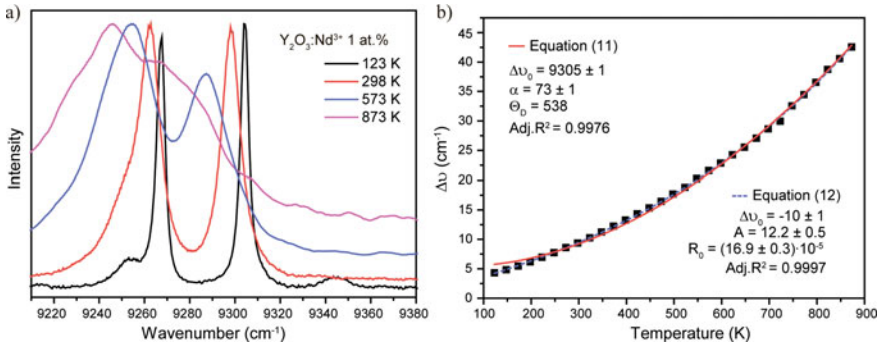

Fig. 5.12 **a** Normalized emission spectra of $^4F_{3/2} - {}^4I_{11/2}$ transition obtained at different temperatures (123–873 K); **b** FWHM of $^4F_{3/2}$ $(R_1) - {}^4I_{11/2}$ (Y_1) transition as a function of temperature [71]

noteworthy that the temperature resolution was found using acquisition and analysis of consecutive photoluminescence spectra.

5.6 Lifetime Thermometry

In contrast to the temperature readout from the intensity of a single emission line, the determination of temperature from the emission lifetime is not really compromised by changes in measurement conditions. Additionally, it is not affected by the inhomogeneity of the probe material. Lifetime measurements have better detection limits than the measurements of intensity, which is important for high-temperature applications and, generally, they present smaller uncertainties compared to those in measurements of intensity [75]. Lifetime-based thermometry, like the ratiometric intensity method, is self-referencing, but it needs the observation of just one emission line. The drawbacks of lifetime measurements are that they require relatively expensive equipment, and, compared to the emission intensity, a longer time to collect experimental data and a more complex processing of emission decay data to derive lifetime values. In addition, the temperature change of the excited state lifetime of rare earth ions generally shows two regimes, which can be easily understood from following equation:

$$\tau(T) = \frac{\tau_r(T)}{1 + \tau_r(T) \cdot k_{nr}(T)} \tag{5.13}$$

where τ and τ_r are the observed and radiative lifetime, k_{nr} is nonradiative decay rate. At low temperatures, where the values of the nonradiative rate are negligible, the lifetime is equal to the radiative lifetime, $\tau \cong \tau_r$. The radiative lifetime only slightly changes with temperature: $\tau_r(T) = \tau_{r0} exp(-\alpha T)$, where α is the phenomenological parameter of order 10^{-4} K^{-1} or less. Therefore, at low temperatures, lifetime only slightly decreases with temperature increase or does not change at all. As a consequence, the lifetime method is practically insensitive to temperature changes in this range. At higher temperatures, the nonradiative decay rate sharply increases, leading to a steep decrease in observed lifetime. The temperature point of the transition between two regions essentially depends on the energy difference between excited levels of rare earth ions and the closest lower energy level or charge-transfer band, and on the phonon energy of the host material. Examples of lifetime temperature dependences of some rare earth-doped metal oxides and salts are shown in Fig. 5.13. The temperature region of lifetime insensitivity presents a major obstacle to its use. This region frequently covers the physiologically relevant temperature range and thus prevents the use of the majority of lifetime based thermal sensors in biomedicine. On the other hand, in the high temperature region, lifetime method is very sensitive. It is worthy of note that the uncertainties in decay times are generally smaller than those in emission intensities and that the current technology facilitates measurements of very short decay times. Therefore, the lifetime sensing technique has the potential

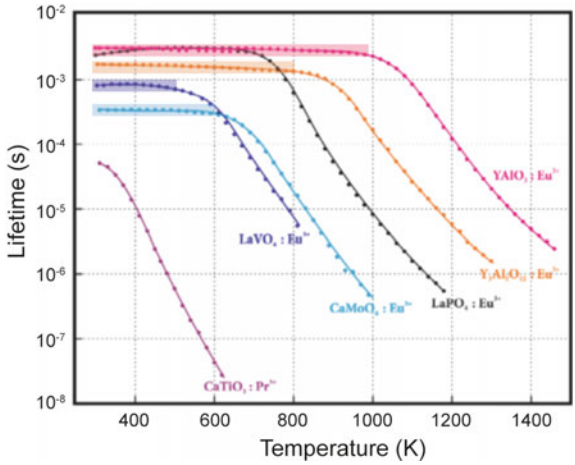

Fig. 5.13 Temperature dependences of lifetime of some lanthanide-doped metal oxides and salts. Shadowed areas show temperature insensitive regions [76]

to present better temperature resolutions than intensity-based measurements and has larger high-temperature operating bounds.

By analyzing the data from Fig. 5.13, one can conclude that Pr^{3+} ions display better lifetime temperature dependence in 300–400 K range compared with Eu^{3+} ions. $LiPr(PO_3)_4$ was tested by Gharouel et al. as lifetime-based contactless thermometer within 298–363 K temperature range [77]. Emission spectra of $LiPr(PO_3)_4$ sample normalized to $^3P_0$–$^3F_2$ transition as a function of temperature obtained upon laser excitation at 488 nm are presented in Fig. 5.14a. In this wavelength region, there are two distinct emission bands attributed to the $^3P_0$–$^3H_6$ and $^3P_0$–$^3F_2$ transitions respectively. The temperature increase results in a more pronounced decline in $^3P_0$–$^3H_6$ intensity compared with that of $^3P_0$–$^3F_2$. Fluorescence decay curves from $^3P_0$ energy level of Pr^{3+} ions registered at different temperatures upon pulsed laser excitation at 488 nm are shown in Fig. 5.14b. The luminescence decay curves demonstrated an exponential behavior in the entire temperature range. Figure 5.14c represents the temperature evolution of the normalized decay time, $\tau_{norm}(T)$, defined

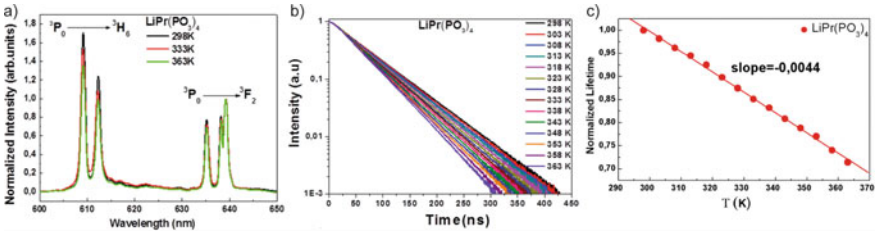

Fig. 5.14 **a** Emission spectra of $LiPr(PO_3)_4$ sample as a function of temperature obtained under laser excitation at 488 nm, **b** fluorescence decay curves of $^3P_0$ level recorded at different temperatures upon 488 nm laser excitation, **c** normalized $^3P_0$ lifetime as a function of the temperature [77]

as $\tau_{norm}(T) = \tau(T)/\tau$ (298 K). The luminescence lifetimes versus temperature monotonically decreased in 298–363 K temperature range and followed a linear behavior ($\tau = a + bT$).

Lifetime-based thermal sensitivity of $LiPr(PO_3)_4$ sample was 0.62% K^{-1}, which was approximately in the same order of magnitude than the sensitivities of previously investigated praseodymium and chromium-doped lifetime based thermometers (0.59% K^{-1} for $NaPr(PO_3)_4$, 0.50% K^{-1} for Cr^{3+}:$Y_3Al_5O_{12}$, 0.83% K^{-1} for Cr^{3+}:$LiAl_5O_8$). The temperature resolution of $LiPr(PO_3)_4$ was determined to be 0.8 K, much higher than those obtained for different lifetime thermometeric sensors such as BaClF:Sm^{3+} ($\Delta T = 5$ °C) [78], Er^{3+}-doped fibers ($\Delta T = 4$ °C) [79], and Cr^{3+}:Al_2O_3 ($\Delta T \approx 2.4$ K) [80].

5.7 Conclusion and Perspectives

The analysis presented in the chapter demonstrated that temperature has become a measurable characteristic at micro- and nanoscale owing to the colossal progress in the technique of luminescence thermometry. The luminescence thermometry relies on high thermal sensitivity of luminescence characteristics such as luminescence intensity, spectral line position, bandwidth, and excited state lifetime, of various materials—from organic dyes to rare earth-doped nanophosphors. The latter objects seem to be the most promising among others. They provide a wide measurable temperature range (from cryogenic to technological values) due to narrow emission lines, high thermal and chemical stability. The current record parameters of luminescence temperature sensors combine high relative thermal sensitivity (> 1% K^{-1}), thermal resolution (~ 0.1 °C) and spatial resolution (< 10 μm) with short acquisition times (< 100 ms). These high performance features are provided both by the use of rare earth-doped phosphors as temperature sensors and by the ratiometric thermometry approach that exploits the relative change in the intensity ratio of two energy-close transitions. The important feature of the ratiometric thermometry discussed in the chapter is the consideration of the thermodynamically quasi-equilibrium state, the so called thermally coupled levels, with energy difference from 200 to 2000 cm^{-1}. In practice, the ratiometric approach can be realized by excited or ground electronic energy levels and two Stark sublevels. Moreover, various readout strategies can be used, such as peak-to-peak and peak-to-valley ratios. Other variants of readout strategy can be realized by means of monitoring the spectral position of the emission lines, bandwidth, and lifetime. Each strategy offers its own advantage and applicability in the specific field.

In such a way, the progress of luminescence thermometry resulted in the creation of breakthrough technologies in various areas of application such as micro- and nanoelectronics, micro- and nanofluidics, photonics, and nanomedicine. As a feedback of the technological progress, new challenges towards luminescence temperature sensors appeared that are connected with requests for further improvement of parameters and broadening of the areas of application. In spite of the already achieved and

extraordinary temperature performance of luminescence thermal sensors, there are urgent tasks that can be prioritized. First of all, the spectral range of the luminescence thermometry has to be widened to NIR emissions correlated with optical windows in biological tissues that is of great importance to application in biomedicine. Another interesting problem to be solved is connected with the fundamental development of the luminescence thermometry by considering alternative strategies such as ratiometric approach based on non-thermally coupled levels and the use of multiple emission centers (couples of different rare earth ions or combinations of rare earth ions with other luminescent elements). The next very ambitious and very promising task is combining the fields of luminescence microscopy and luminescence thermometry. The current achievements of luminescence microscopy allow visualization of objects below the resolution of a light microscope, resulting in in vivo noninvasive study of ongoing biological processes and 3D optical tomographic reconstructions. Integration of luminescence microscopy and thermometry in mutual technological protocol will provide multimodal spectral diagnostics with potency of 3D visualization and thermal mapping with micro- and nanoscale resolution. It should be noted that other variants of dual- or multi-sensing devices with thermometric functionalities are also promising and realizable. Further progress in fundamental and applied luminescence thermometry is inevitably approaching.

Acknowledgements This research has been performed in "Center for Optical and Laser materials research".

References

1. P.R.N. Childs, J.R. Greenwood, C.A. Long, Review of temperature measurement. Rev. Sci. Instrum. **71**, 2959–2978 (2000)
2. C.D.S. Brites, A. Millán, L.D. Carlos, Lanthanides in luminescent thermometry. Handb. Phys. Chem. Rare Earths **49**, 339–427 (2016). https://doi.org/10.1016/bs.hpcre.2016.03.005
3. C.D.S. Brites, P.P. Lima, N.J.O. Silva et al., Thermometry at the nanoscale. Nanoscale **4**, 4799–4829 (2012). https://doi.org/10.1039/c2nr30663h
4. D. Jaque, F. Vetrone, Luminescence nanothermometry. Nanoscale **4**, 4301 (2012). https://doi.org/10.1039/c2nr30764b
5. X. Wang, O.S. Wolfbeis, R.J. Meier, Luminescent probes and sensors for temperature. Chem. Soc. Rev. **42**, 7834–7869 (2013)
6. S. Uchiyama, A. Prasanna de Silva, K. Iwai, Luminescent molecular thermometers. J. Chem. Educ. **83**, 720 (2006)
7. Y. Yue, X. Wang, Nanoscale thermal probing. Nano Rev. **3**, 11586 (2012)
8. S. Uchiyama, N. Kawai, A.P. de Silva, K. Iwai, Fluorescent polymeric AND logic gate with temperature and pH as inputs. J. Am. Chem. Soc. **126**, 3032–3033 (2004)
9. K. Okabe, N. Inada, C. Gota et al., Intracellular temperature mapping with a fluorescent polymeric thermometer and fluorescence lifetime imaging microscopy. Nat. Commun. **3**, 705 (2012)
10. J.S. Donner, S.A. Thompson, M.P. Kreuzer et al., Mapping intracellular temperature using green fluorescent protein. Nano Lett. **12**, 2107–2111 (2012)
11. P. Löw, B. Kim, N. Takama, C. Bergaud, High-spatial-resolution surface-temperature mapping using fluorescent thermometry. Small **4**, 908–914 (2008)

12. C. Paviolo, A.H.A. Clayton, S.L. McArthur, P.R. Stoddart, Temperature measurement in the microscopic regime: a comparison between fluorescence lifetime-and intensity-based methods. J. Microsc. **250**, 179–188 (2013)
13. H.D.A. Santos, D. Ruiz, G. Lifante et al., Time resolved spectroscopy of infrared emitting Ag_2S nanocrystals for subcutaneous thermometry. Nanoscale **9**, 2505–2513 (2017)
14. S. Kalytchuk, O. Zhovtiuk, S.V. Kershaw et al., Temperature-dependent exciton and trap-related photoluminescence of CdTe quantum dots embedded in a NaCl matrix: implication in thermometry. Small **12**, 466–476 (2016)
15. J. Ueda, M. Back, M.G. Brik et al., Ratiometric optical thermometry using deep red luminescence from $^4T_2$ and ^2E states of Cr^{3+} in $ZnGa_2O_4$ host. Opt. Mater. (Amst) **85**, 510–516 (2018)
16. E. Glais, V. Đorđević, J. Papan et al., $MgTiO_3$: Mn^{4+} a multi-reading temperature nanoprobe. RSC Adv. **8**, 18341–18346 (2018)
17. A. Benayas, B. del Rosal, A. Pérez-Delgado et al., Nd: YAG near-infrared luminescent nanothermometers. Adv. Opt. Mater. **3**, 687–694 (2015)
18. L. Marciniak, A. Bednarkiewicz, K. Elzbieciak, NIR–NIR photon avalanche based luminescent thermometry with Nd^{3+} doped nanoparticles. J. Mater. Chem. C **6**, 7568–7575 (2018)
19. O. Savchuk, J.J. Carvajal, L.G. De la Cruz et al., Luminescence thermometry and imaging in the second biological window at high penetration depth with Nd:KGd $(WO_4)_2$ nanoparticles. J. Mater. Chem. C **4**, 7397–7405 (2016)
20. I.E. Kolesnikov, E.V. Golyeva, E. Lähderanta et al., Ratiometric thermal sensing based on Eu^{3+}-doped YVO4 nanoparticles. J. Nanopart. Res. **18**, 354 (2016). https://doi.org/10.1007/s11051-016-3675-8
21. J.-C.G. Buenzli, S.V. Eliseeva, Intriguing aspects of lanthanide luminescence. Chem. Sci. **4**, 1939–1949 (2013)
22. K. Binnemans, Lanthanide-based luminescent hybrid materials. Chem. Rev. **109**, 4283–4374 (2009)
23. J. Feng, H. Zhang, Hybrid materials based on lanthanide organic complexes: a review. Chem. Soc. Rev. **42**, 387–410 (2013)
24. C.D.S. Brites, P.P. Lima, N.J.O. Silva et al., A luminescent molecular thermometer for long-term absolute temperature measurements at the nanoscale. Adv. Mater. **22**, 4499–4504 (2010). https://doi.org/10.1002/adma.201001780
25. Z. Wang, D. Ananias, A. Carné-Sánchez et al., Lanthanide-organic framework nanothermometers prepared by spray-drying. Adv. Funct. Mater. **25**, 2824–2830 (2015)
26. J. Rocha, C.D.S. Brites, L.D. Carlos, Lanthanide organic framework luminescent thermometers. Chem. Eur. J. **22**, 14782–14795 (2016)
27. S. Arai, S. Takeoka, S. Ishiwata et al., Micro-thermography in millimeter-scale animals by using orally-dosed fluorescent nanoparticle thermosensors. Analyst **140**, 7534–7539 (2015)
28. E.N. Cerón, D.H. Ortgies, B. del Rosal et al., Hybrid nanostructures for high-sensitivity luminescence nanothermometry in the second biological window. Adv. Mater. **27**, 4781–4787 (2015). https://doi.org/10.1002/adma.201501014
29. O.A. Savchuk, P. Haro-Gonzalez, J.J. Carvajal et al., Er:Yb:NaY_2F_5O up-converting nanoparticles for sub-tissue fluorescence lifetime thermal sensing. Nanoscale **6**, 9727–9733 (2014)
30. K. Trejgis, A. Bednarkiewicz, L. Marciniak, Engineering excited state absorption based nanothermometry for temperature sensing and imaging. Nanoscale **12**, 4667–4675 (2020)
31. I.E. Kolesnikov, E.V. Golyeva, M.A. Kurochkin et al., Nd^{3+}-doped YVO4 nanoparticles for luminescence nanothermometry in the first and second biological windows. Sens. Actuators B Chem. **235**, 287–293 (2016). https://doi.org/10.1016/j.snb.2016.05.095
32. I.E. Kolesnikov, A.A. Kalinichev, M.A. Kurochkin et al., New strategy for thermal sensitivity enhancement of Nd^{3+}-based ratiometric luminescence thermometers. J. Lumin. **192**, 40–46 (2017). https://doi.org/10.1016/j.jlumin.2017.06.024
33. R. Alicki, D.M. Leitner, Size-dependent accuracy of nanoscale thermometers. J. Phys. Chem. B **119**, 9000–9005 (2015)

34. G. Tóth, I. Apellaniz, Quantum metrology from a quantum information science perspective. J. Phys. A Math. Theor. **47**, 424006 (2014)
35. A.A. Alaulamie, Nanoscale temperature measurement of phase transition in water using novel optical thermometry techniques (2017)
36. J.W. Bartlett, C. Frost, Reliability, repeatability and reproducibility: analysis of measurement errors in continuous variables. Ultrasound Obstet. Gynecol. Off. J. Int. Soc. Ultrasound Obstet. Gynecol. **31**, 466–475 (2008)
37. B.N. Taylor, C.E. Kuyatt, Guidelines for evaluating and expressing the uncertainty of NIST measurement results (1994)
38. S.A. Wade, S.F. Collins, G.W. Baxter, Fluorescence intensity ratio technique for optical fiber point temperature sensing. J. Appl. Phys. **94**, 4743–4756 (2003)
39. M.D. Shinn, W.A. Sibley, M.G. Drexhage, R.N. Brown, Optical transitions of Er^{3+} ions in fluorozirconate glass. Phys. Rev. B **27**, 6635 (1983)
40. S.F. León-Luis, U.R. Rodríguez-Mendoza, P. Haro-González et al., Role of the host matrix on the thermal sensitivity of Er^{3+} luminescence in optical temperature sensors. Sens. Actuators B Chem. **174**, 176–186 (2012)
41. A.H. Khalid, K. Kontis, 2D surface thermal imaging using rise-time analysis from laser-induced luminescence phosphor thermometry. Meas. Sci. Technol. **20**, 25305 (2009)
42. A.A. Kalinichev, M.A. Kurochkin, E.V. Golyeva et al., Near-infrared emitting YVO4:Nd^{3+} nanoparticles for high sensitive fluorescence thermometry. J. Lumin. **195**, 61–66 (2018). https://doi.org/10.1016/j.jlumin.2017.11.024
43. I.E. Kolesnikov, D.V. Tolstikova, A.V. Kurochkin et al., Concentration effect on structural and luminescent properties of YVO_4:Nd^{3+} nanophosphors. Mater. Res. Bull. **70**, 799–803 (2015). https://doi.org/10.1016/j.materresbull.2015.06.023
44. J.B. Gruber, D.K. Sardar, K.L. Nash, R.M. Yow, Comparative study of the crystal-field splitting of trivalent neodymium energy levels in polycrystalline ceramic and nanocrystalline yttrium oxide. J. Appl. Phys. **102**, 23103 (2007)
45. S. Balabhadra, M.L. Debasu, C.D.S. Brites et al., Boosting the sensitivity of Nd^{3+}-based luminescent nanothermometers. Nanoscale **7**, 17261–17267 (2015)
46. X. Tian, X. Wei, Y. Chen et al., Temperature sensor based on ladder-level assisted thermal coupling and thermal-enhanced luminescence in $NaYF_4$:Nd^{3+}. Opt. Express **22**, 30333–30345 (2014)
47. W. Xu, Q. Song, L. Zheng et al., Optical temperature sensing based on the near-infrared emissions from Nd^{3+}/Yb^{3+} codoped $CaWO_4$. Opt. Lett. **39**, 4635–4638 (2014)
48. G. Jiang, X. Wei, S. Zhou et al., Neodymium doped lanthanum oxysulfide as optical temperature sensors. J. Lumin. **152**, 156–159 (2014)
49. U. Rocha, C. Jacinto da Silva, W. Ferreira Silva et al., Subtissue thermal sensing based on neodymium-doped LaF_3 nanoparticles. ACS Nano **7**, 1188–1199 (2013)
50. L. Marciniak, K. Prorok, A. Bednarkiewicz et al., Water dispersible $LiNdP_4O_{12}$ nanocrystals: new multifunctional NIR–NIR luminescent materials for bio-applications. J. Lumin. **176**, 144–148 (2016). https://doi.org/10.1016/j.jlumin.2016.03.034
51. I.E. Kolesnikov, A.A. Kalinichev, M.A. Kurochkin et al., Structural, luminescence and thermometric properties of nanocrystalline YVO_4:Dy^{3+} temperature and concentration series. Sci. Rep. **9**, 2043 (2019). https://doi.org/10.1038/s41598-019-38774-6
52. Z. Cao, S. Zhou, G. Jiang et al., Temperature dependent luminescence of Dy^{3+} doped $BaYF_5$ nanoparticles for optical thermometry. Curr. Appl. Phys. **14**, 1067–1071 (2014)
53. S. Ćulubrk, V. Lojpur, S.P. Ahrenkiel et al., Non-contact thermometry with Dy^{3+} doped $Gd_2Ti_2O_7$ nano-powders. J. Lumin. **170**, 395–400 (2016)
54. L.M. Chepyga, A. Osvet, C.J. Brabec, M. Batentschuk, High-temperature thermographic phosphor mixture YAP/YAG:Dy^{3+} and its photoluminescence properties. J. Lumin. **188**, 582–588 (2017)
55. B.R. Anderson, R. Gunawidjaja, H. Eilers, Dy^{3+}-doped yttrium complex molecular crystals for two-color thermometry in heterogeneous materials. J. Lumin. **188**, 238–245 (2017)

56. I.E. Kolesnikov, A.A. Kalinichev, M.A. Kurochkin et al., Ratiometric optical thermometry based on emission and excitation spectra of YVO_4:Eu^{3+} nanophosphors. J. Phys. Chem. C **123**, 5136–5143 (2019)
57. I.E. Kolesnikov, A.A. Kalinichev, M.A. Kurochkin et al., Y_2O_3:Nd^{3+} nanocrystals as ratiometric luminescence thermal sensors operating in the optical windows of biological tissues. J. Lumin. **204**, 506–512 (2018). https://doi.org/10.1016/j.jlumin.2018.08.050
58. I.E. Kolesnikov, E.V. Golyeva, A.A. Kalinichev et al., Nd^{3+} single doped YVO_4 nanoparticles for sub-tissue heating and thermal sensing in the second biological window. Sens. Actuators B Chem. **243**, 338–345 (2017). https://doi.org/10.1016/j.snb.2016.12.005
59. E. Carrasco, B. del Rosal, F. Sanz-Rodríguez et al., Intratumoral thermal reading during photothermal therapy by multifunctional fluorescent nanoparticles. Adv. Funct. Mater. **25**, 615–626 (2015). https://doi.org/10.1002/adfm.201403653
60. A. Benayas, B. del Rosal, A. Pérez-Delgado et al., Nd:YAG near-infrared luminescent nanothermometers. Adv. Opt. Mater. **3**, 687–694 (2015). https://doi.org/10.1002/adom.201400484
61. U. Rocha, C. Jacinto, K.U. Kumar et al., Real-time deep-tissue thermal sensing with sub-degree resolution by thermally improved Nd^{3+}:LaF_3 multifunctional nanoparticles. J. Lumin. **175**, 149–157 (2016). https://doi.org/10.1016/j.jlumin.2016.02.034
62. B. del Rosal, E. Ximendes, U. Rocha, D. Jaque, In vivo luminescence nanothermometry: from materials to applications. Adv. Opt. Mater. **5**, 1600508 (2017)
63. S.A. Johnson, H.G. Freie, A.L. Schawlow, W.M. Yen, Thermal shifts in the energy levels of LaF_3:Nd^{3+}. JOSA **57**, 734–737 (1967)
64. T. Kushida, Linewidths and thermal shifts of spectral lines in neodymium-doped yttrium aluminum garnet and calcium fluorophosphate. Phys. Rev. **185**, 500–508 (1969). https://doi.org/10.1103/PhysRev.185.500
65. Ł Marciniak, A. Bednarkiewicz, D. Hreniak, W. Strek, The influence of Nd^{3+} concentration and alkali ions on the sensitivity of non-contact temperature measurements in $ALaP_4O_{12}$:Nd^{3+} (A = Li, K, Na, Rb) nanocrystalline luminescent thermometers. J. Mater. Chem. C **4**, 11284–11290 (2016). https://doi.org/10.1039/c6tc03396b
66. X. Chen, B. Di Bartolo, Phonon effects on sharp luminescence lines of Nd^{3+} in $Gd_3Sc_2Ga_3O_{12}$ garnet (GSGG). J. Lumin. **54**, 309–318 (1993)
67. A. Kiel, Temperature-dependent line width of excited states in crystals. I. Line broadening due to adiabatic variation of the local fields. Phys. Rev. **126**, 1292 (1962)
68. D.K. Sardar, R.M. Yow, Inter-stark energy levels and effects of temperature on sharp emission lines of Nd^{3+} in $LiYF_4$. Phys. Status Solidi A Appl. Res. **173**, 521–534 (1999)
69. D.K. Sardar, R.M. Yow, Optical characterization of inter-stark energy levels and effects of temperature on sharp emission lines of Nd^{3+} in $CaZn_2Y_2Ge_3O_{12}$. Opt. Mater. (Amst) **10**, 191–199 (1998)
70. I.E. Kolesnikov, A.A. Kalinichev, M.A. Kurochkin et al., YVO_4:Nd^{3+} nanophosphors as NIR-to-NIR thermal sensors in wide temperature range. Sci. Rep. **7**, 18002 (2017). https://doi.org/10.1038/s41598-017-18295-w
71. I.E. Kolesnikov, A.A. Kalinichev, M.A. Kurochkin et al., Bifunctional heater-thermometer Nd^{3+}-doped nanoparticles with multiple temperature sensing parameters. Nanotechnology **30**, 145501 (2019). https://doi.org/10.1088/1361-6528/aafcb8
72. D.K. Sardar, R.M. Yow, Stark components of $^4F_{3/2}$, $^4I_{9/2}$ and $^4I^{11/2}$ manifold energy levels and effects of temperature on the laser transition of Nd^{3+} in YVO_4. Opt. Mater. (Amst) **14**, 5–11 (2000)
73. B. Di Bartolo, R.H. Silsbee, Optical interactions in solids. Am. J. Phys. **37**, 756–757 (1969)
74. D.W. Posener, The shape of spectral lines: tables of the Voigt profile. Aust. J. Phys. **12**, 184–196 (1959)
75. M.D. Chambers, D.R. Clarke, Doped oxides for high-temperature luminescence and lifetime thermometry. Annu. Rev. Mater. Res. **39**, 325–359 (2009)
76. J. Brübach, C. Pflitsch, A. Dreizler, B. Atakan, On surface temperature measurements with thermographic phosphors: a review. Prog. Energy Combust. Sci. **39**, 37–60 (2013)

77. S. Gharouel, L. Labrador-Páez, P. Haro-González et al., Fluorescence intensity ratio and lifetime thermometry of praseodymium phosphates for temperature sensing. J. Lumin. **201**, 372–383 (2018)
78. J.S. McCormack, Remote optical measurement of temperature using luminescent materials. Electron. Lett. **17**, 630–631 (1981)
79. Z.Y. Zhang, K.T.V. Grattan, A.W. Palmer et al., Fluorescence decay-time characteristics of erbium-doped optical fiber at elevated temperatures. Rev. Sci. Instrum. **68**, 2764–2766 (1997)
80. H.C. Seat, J.H. Sharp, Dedicated temperature sensing with c-axis oriented single-crystal ruby (Cr/sup 3+: Al/sub 2/O/sub 3/) fibers: temperature and strain dependences of R-line fluorescence. IEEE Trans. Instrum. Meas. **53**, 140–154 (2004)